Journal of Colloid and Interface Science 404 (2013) 169–178

Contents lists available at SciVerse ScienceDirect

Journal of Colloid and Interface Science

www.elsevier.com/locate/jcis

One-way wicking in open micro-channels controlled by channel topography

Jiansheng Feng [a], Jonathan P. Rothstein [b,*]

[a] Department of Physics, University of Massachusetts, Amherst, United States
[b] Department of Mechanical and Industrial Engineering, University of Massachusetts, Amherst, MA 01003, United States

ARTICLE INFO

Article history:
Received 27 November 2012
Accepted 22 February 2013
Available online 6 May 2013

Keywords:
Directional wicking
Surface-tension effect
Capillarity
Contact angle
Laplace pressure
Three-dimensional meniscus

ABSTRACT

One-way wicking (microfluidic diode) behaviors of a range of IPA–water mixtures on internally structured PDMS-based open micro-channels were experimentally demonstrated and quantified. The open microfluidic channels, each internally decorated with an array of angled fin-like-structure pairs, were fabricated using a combined photolithography and soft molding procedure. Propagations of wetting fluids were found to be much more impeded on the fin-tilting direction, or the hard wicking direction, comparing to the opposite direction, or the easy wicking direction. This asymmetric wicking behaviors were attributed to the structure-induced direction-dependent Laplace pressure. Two key parameters – the contact angle of the wicking fluid and the tilting angle of the fin-like structures – were studied. The effects of preferential evaporation and wetting instability were also investigated. The findings of this study are expected to provide a better understanding of how fluids interact with micro-scaled structures and to offer a new way of manipulating fluids at the micron and nanometer scales.

1. Introduction

Holding promising prospects for efficient and economic automation and parallelization of fluid-based experiments, microfluidics has emerged as an important experimental platform in the fields of chemistry, biology, medicine research, and material science [1–4]. The micrometer size-scale is the most important characteristics of microfluidics from the application standpoint as well as from the physics standpoint [5]. The rapid growth of microfluidics in recent decades has triggered the need for new strategies to effectively control fluid flow at small scales, where surface forces and viscous forces dominate over gravity and inertia. In order to perform any basic operations within a microfluidic device, one must first be able to move the test fluid. This can be done actively with valves and pumps [6,7], or passively using capillary action [8,9]. At the size-scales of microfluidic channels, viscous and surface-tension effects dominate the behavior of the fluid. As a result, pressure-driven pumping of a fluid through a microfluidic device can often be difficult. Conversely, utilizing capillary action or wicking to move wetting fluids in those devices is typically relatively easy and effective. A number of interesting studies have appeared in the recent literature utilizing wicking to develop low-cost microfluidics platform suitable for chemical and biological sensing and diagnostics [8–11]. These paper-based or thread-based microfluidics devices allow simple transporting and mixing functionality, but are unable to provide a high level of fluidic control.

Chen et al. [12] has reported a paper-based fluidic diode which controls fluid to wick on only one direction. Their devices relied on deposition of surfactant in specific regions on the device during the fabrication process, and therefore they are single use only. Alternatively, we are interested in using structure-induced surface tension effects to control the wicking behavior. It has been demonstrated that uni-directional liquid spreading can be achieved on surfaces decorated with asymmetric structures (*e.g.*, stooped nano-hairs [13], deflected nano-pillars [14]). Chu et al. [14] also developed a theory to explain the uni-directional spreading behavior along the direction of the deflected pillars, which allows for making quantitative predictions of spreading asymmetry based on the combination of water contact angle and deflection angle of the pillars. Blow et al. [15,16] have reported simulation studies that showed anisotropic imbibition of a fluid interacting with an array of hydrophilic polygonal prism structures. They found that the pinning of fluid front had direction-dependency affected by the shape and orientation of the polygonal prisms and the array arrangement. It has been mentioned in a previous study that capillary filling of micro-channels can be impeded by the posts or ridges patterned inside the channels due to contact line pinning [17]. Here we report an experimental study on direction-dependent wicking behavior induced by structural asymmetry in microfluidic channels. The objective of this study was to develop microfluidic diodes based on geometric effects. Specifically, we experimentally

* Corresponding author.
E-mail address: rothstein@ecs.umass.edu (J.P. Rothstein).

0021-9797/$ - see front matter © 2013 Elsevier Inc. All rights reserved.
http://dx.doi.org/10.1016/j.jcis.2013.02.052

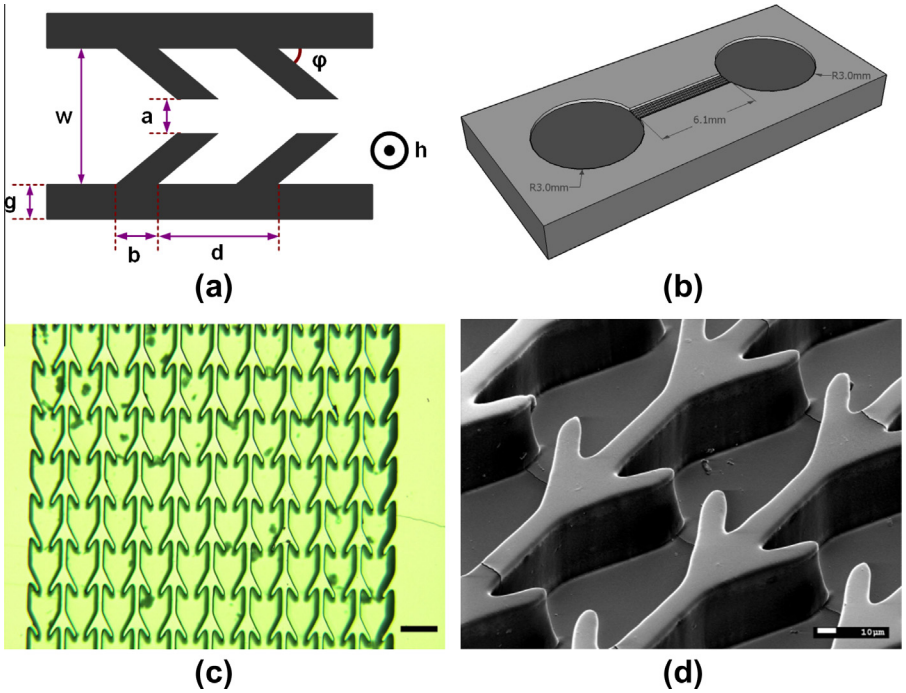

Fig. 1. Schematic diagrams and microscope images of the asymmetric-structure-decorated micro-channels. In (a), schematic diagram of a linear channel with tilted fins on the side-walls is shown. Here only a top view of a small representative section of a single channel is shown with all relevant geometric parameters labeled. In (b), a schematic diagram of a typical open microfluidic device used in this study is shown. In (c), an optical micrograph of a set of ten parallel channels is shown. The scale-bar at the lower-right corner represents 100 μm. In (d), a 45° view SEM image of a small section of the micro-channels on the PDMS device is shown.

demonstrate one-way wicking microfluidic channels by decorating both side-walls of an open linear micro-channel with an array of angled fin-like structures, as shown in Fig. 1a. The direction-dependent Laplace pressure induced in these micro-channels allowed a wetting fluid to wick in a predefined direction while prohibited spreading of the same fluid in the opposite direction. A series of fluids were tested to systematically study the effects of changing surface tension and, as a result, contact angle. The impacts of preferential evaporation and wetting instability were also studied. Finally, a complete three-dimensional (3-D) model were developed to provide quantitative predictions of the wicking behavior governed by geometric effects.

2. Material and methods

2.1. Fabrication

Materials and apparatus: SU-8 2015 and SU-8 2050 resists from MicroChem, CEE 100CB spin-coater from Brewer Science, 3-in. wafers from WRS Materials, MA6 mask-aligner from SUSS MicroTec, HOYA U-350 filter from Newport Glass, plastic film photo-mask from CAD/Art Services, Sylgard-184 silicone elastomer kit from Dow Corning, HMS-301 PDMS crosslinker from Gelest, PGMEA ($\geqslant$99.5%) from Sigma–Aldrich.

The fabrication of microfluidic channels includes two main steps: photolithography and silicone molding. In step one, a standard SU-8 photolithography procedure was performed to generated molding masters with negative structures of the channels. SU-8 2015 resist and SU-8 2050 resist were first spin-coated onto silicon wafers to produce 22 μm-thick and 60 μm-thick SU-8 films, respectively. Then, after a soft bake, the SU-8 coated wafers were exposed in a mask-aligner to 365 nm UV light through a pre-designed photo-mask and a UV filter. Finally, the exposed SU-8 samples went through a post-exposure bake, a PGMEA development, and a hardening bake. The spin-coating speed, soft-bake time, exposure dosage, post-exposure-bake time, development time, and the hardening-bake time all followed the corresponding instructions provided in the SU-8 processing guidelines sheet. In step two, part A (base) of Sylgard-184 was first thoroughly mixed with HMS-301 at an approximately 16:1 volume ratio. The mixture was then degassed in a vacuum chamber and slowly cast onto the masters that were individually seated in polystyrene Petri dishes. The mixtures filled up to approximately 2 mm above the top surface of the masters. These Preti dishes were then covered and left on a level platform for a slow curing at room temperature overnight (more than twelve hours) followed by a completion of curing at 80 °C for two hours. Finally, the samples were slowly cooled down and the silicone devices were carefully separated from the SU-8 masters.

2.2. Wicking experiments

Materials and apparatus: Isopropyl alcohol ($\geqslant$99.9%) from Fisher Scientific, RO-water from a Millipore Milli-Q system, EO-1312C CMOS Color USB camera and 50 mm spacer from Edmund Optics, V5018 video lens (50 mm, F/1.8) from Computar, Eclipse TE2000-U microscope system with CFL Plan Fluor 10X objective lens and LHS-H100C-1 light source from Nikon, Phantom V4.4 high-speed video camera with PH607 video processing software from Vision Research, KDS100 syringe pump from KD Scientific, 1 mL Norm-Ject disposable syringes from Henke-Sass Wolf, Intramedic polyethylene tubing from Clay Adams.

Each PDMS device was first cut and carefully placed on a piece of clean glass slide. Before each experiment, the device surface were cleaned with abundant amount of RO-water and dried with compressed air. In an wicking characterization experiment, the glass slide (with device on top) was placed on top of a leveled diffused light source. The Edmund video camera was set up above the device at an angle between 35° and 45° from horizontal. Deposition of test fluids were performed at a constant speed with a

syringe pump. Total duration of the fluid deposition was between 1.5 s and 3.0 s depending on the target volume. For experiments in closed atmosphere, the whole glass slide was covered with a transparent polystyrene Petri dish with drilled holes for needle access. For observations of the fluid propagation, the Phantom high-speed video camera was set up on the Nikon optical microscope to capture videos of fluid front propagation at 1000 fps with 512×512 pixels resolution. All experiments were done under room temperature of 21.0 °C ± 2.0 ° C.

2.3. Microscopy

Materials and apparatus: Cressington 108 sputter coater from Ted Pella, JSM-7001F Thermal FE-SEM from JEOL, Olympus BH2 Microscope with Infinity 2 digital camera.

All SU-8 masters and PDMS devices were examined with optical microscopy. Some of the PDMS devices were also examined by Scanning Electron Microscopy (SEM) after wicking experiments. For SEM examinations, small sections of the PDMS devices were first sputtered with a thin layer of gold (~ 50 nm) on the surface. SEM imaging were performed under high vacuum at 5.0 kV acceleration voltage and ~160 pA current.

3. Results and discussion

A series of microfluidic devices consisting of ten parallel micro-channels (length ~6 mm) side-by-side with each end connected to a reservoir (diameter ~6 mm) were fabricated via a combined process of photolithography and soft molding [18,19]. A schematic diagram of the microfluidic device is shown in Fig. 1b. The geometry of a straight channel was modified through the addition of asymmetric side structures to induce asymmetric wicking. The size, orientation, and spacing of the tilted fins shown in Fig. 1a were modified over a wide range, and optimized to maximize the speed of wicking and the degree of asymmetry. Table 1 lists the range of structural parameters used in the photo-mask design, as well as the optimized value for the device shown in Fig. 1c and d. Although experimental data exist for all the designs outlined in Table 1, for brevity and clarity, only the results of the optimized channel are presented in detail here.

Representative images of the micro-structures of a small section of the parallel channels are shown in Fig. 1c and d. As expected, only small deviations of the fabricated structures were observed from the original photomask's design patterns. The height of the micro-structures on the device, as measured with optical profilometry and SEM imaging, was determined to be 56 ± 1 μm. Details of the fabrication and characterization procedures are explained in the experimental section. The product devices were formed in the surface of cured Sylgard-184, a silicone material commonly referred to as PDMS. Wicking tests were carried out directly on these open microfluidic devices by slowly depositing a precise amount of test fluid onto the reservoirs and allowing it to spontaneously spread into the micro-channels. No additional surface treatment or sealing of the top of the device were performed prior to the tests. PDMS is mildly hydrophobic with an advancing contact angle of $\theta_{water} \approx 102°$, but PDMS is wet by IPA which has a contact angle of $\theta_{IPA} \approx 33°$. Mixtures of IPA and RO-water were made with advancing contact angles between those two limits to systematically probe the effect of contact angle on wicking rates and degree of asymmetry. Alternatively, the advancing contact angle could have been changed by modifying the surface chemistry of the device through silane chemistry. This is particularly relevant to biomedical applications where water or saline are used as the working fluid.

Table 1
Values of the structural parameters of wicking devices studied. These parameters are defined in Fig. 1a.

Parameter	w (μm)	a (μm)	b (μm)	d (μm)	g (μm)	h (μm)	ϕ (°)
Range of values	80–90	20–30	20–40	100–120	20	22–56	27–45
Optimized device	80	20	40	120	20	56	27

The initial experimental demonstration of asymmetric wicking in our "microfluidic diodes" was performed with a mixture of 80% by volume IPA and 20% RO-water as the test fluid. In Fig. 2, two time-lapse images are presented side-by-side to show the test fluid wicking through the micro-channels in opposite directions. These images represent two separate experiments. In each case, the volume of deposited fluid was set to be 15.0 μL. As seen in Fig. 2, the wetting behavior of an identical fluid can be quite different depending on which direction it wicks. On the left-hand-side, the wetting fluid spread rapidly along the channels, and within ten seconds, the fluid covered the entire length of the micro-channels. We denote this as the easy wicking direction because a wetting fluid can spread readily. The easy wicking direction was found to be opposite to the tilting direction of the fin-like structures inside the channels. On the right-hand-side, the same wetting fluid hardly penetrated into the channels because its spreading front was strongly pinned at the corners of the tilted fins added near the entrance of the micro-channels. We denote this as the hard wetting direction. Experiments with 20.0 μL, 25.0 μL, and 30.0 μL test fluids were performed to determine whether varying the amount of test fluid deposited onto the reservoir had an effect on the one-way wicking behavior. It was found that, as long as the overflow (i.e., the distance between the foot of bulk droplet and the entrance of channels) was subtracted as background, the speed and distance a given fluid front was observed to wick into the channel was independent of drop size in the reservoir.

During the entire study, care was taken to ensure that the wicking experiments in opposite directions of the same set of micro-channels were performed under consistent conditions, so that valid comparisons could be drawn. Specifically, the PDMS devices were cleaned and dried with the same procedure before each tests, the same amount of test fluids were deposited with the same manner, and the temperature, lighting, and air flow conditions were kept as consistent as possible. To examine repeatability of the wicking behavior, multiple experiments with identical experimental parameters were performed and compared. Moreover, multiple devices duplicated (negatively) from a single SU-8 master wafer were also tested and compared. No difference of statistical significance was observed in either set of comparisons.

The effect of surface tension in a fluid system is exhibited in the form of the Laplace pressure. Mathematically, the magnitude and direction Laplace pressure can be calculated by knowing the local curvature of a given point on a surface such that

$$\Delta P = \gamma \vec{\nabla} \cdot \hat{n} = \gamma \left(\frac{1}{R_1} + \frac{1}{R_2} \right). \tag{1}$$

Here $\hat{n}$ is the local unit normal vector, $1/R_1$ and $1/R_2$ are the two principle curvatures. This indicates that balancing of surface forces or minimization of surface energy is intrinsically a geometry problem. As a result, because the fluid dynamics is dictated by forces, it is possible to use the geometric design of the micro-channels to control the wicking behavior of the test fluid [15–17]. The key concept in this physical model is the recognition that, at small characteristic length-scale (i.e., the width of the micro-channels), the interfacial forces are large comparing to inertial forces and gravitational forces. This can be demonstrated through the formulation of a

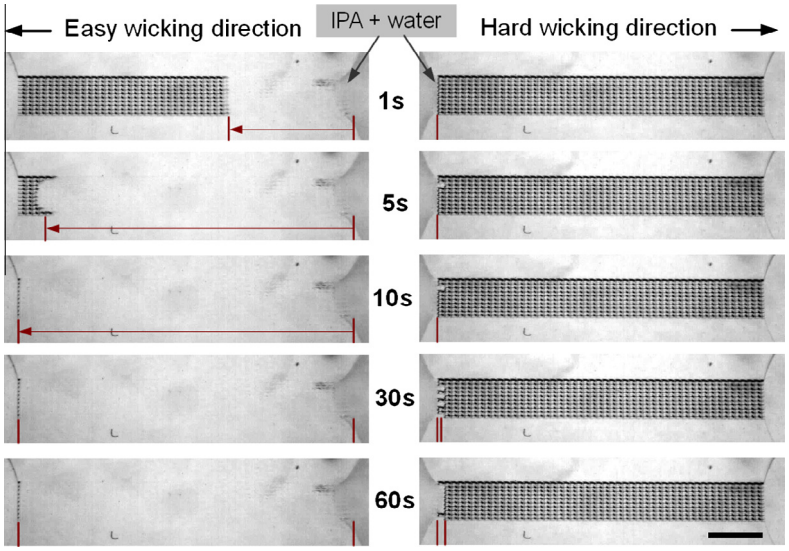

Fig. 2. Time-lapse images of wicking of the same fluid, 80% IPA+ 20% H_2O solution, on opposite directions along the same set of micro-channels demonstrate one-way wicking behavior of the system. In both cases, the fluid front wicked from the center outward. The scale-bar at the lower-right corner represents 1.0 mm.

number of different dimensionless groups. Here the Reynolds number, $Re_{max} = \rho V w/\mu \approx 0.4$, which quantifies the relative strength of inertial forces comparing to viscous forces, is small; the Bond number, $Bo_{max} = \rho g \ w^2/\gamma \approx 3 \times 10^{-3}$, which quantifies the relative strength of gravity comparing to interfacial forces, is small; and the capillary length, which is $\kappa_{min}^{-1} = \sqrt{\gamma/(\rho g)} \approx 1.5$ mm for the IPA water mixtures, is large compared to the dimensions of the features in the micro-channels. While it may not represent a sharp transition, the capillary length provides an order-of-magnitude estimate of the length scale below which interfacial effects become dominant. For these calculations, $\rho = 1.0 \times 10^3$ kg/m^3 is the density of water, $\mu = 1.0 \times 10^{-3}$ Pa·s is the dynamic viscosity of water, $\gamma = 22 \times 10^{-3}$ N/m is the surface tension of isopropanol, $w = 80$ μm is the width of the micro-channels, and $V_{max} = 1.0$ cm/s is the estimated maximum velocity of the fluid.

The one-way wicking phenomenon explored in this study resulted from the ability of the micro-structured channels to locally impose different boundary conditions on the spreading front (or meniscus) in opposite spreading directions. To qualitatively explain this mechanism, a simplified two-dimensional (2D) model is presented in Fig. 3. In this figure, the top-view images of the spreading meniscus at different stages of propagation on both the easy (left-hand side) and the hard (right-hand side) wicking directions are listed with the strength and direction of the pressure gradient at each stage represented by the arrow placed at the corresponding moving contact line. Here we assume that a wetting fluid (shown in blue) meets the side walls of the micro-channels and of the internal fin-like structures (shown in black) at a constant advancing contact angle, which is less than 90°. The spreading of this fluid can easily continue in either direction when the front is in the straight section connecting the tilted fins (Fig. 3a and d) or when it is entering the narrow opening between the tilted fins on opposite walls (Fig. 3b and e) because the curvature of the meniscus in these cases remains negative which results in a pressure gradient aligned in the flow direction. The decisive stage is when the spreading front exits the tilted fin pairs (Fig. 3f and c). In the hard wicking direction, the fluid front must form a convex meniscus. This results in a pressure gradient that resists further spreading and pins the contact line. In the easy wicking direction, the shape of the meniscus downstream of the tilted fins can be either concave or convex depending on whether $\phi + \theta < 90°$ (concave) or $\phi + \theta > 90°$ (convex), where ϕ is the tilting angle, and θ is the advancing contact angle. Consequently, with simple addition of a tilted-fin geometry to an open micro-channel, this 2D model demonstrates how asymmetric wicking can be achieved. As we will see later, this simple 2D model cannot quantitatively explain all our observations. In some cases, 3D effects must be considered.

To examine the proposed 2D model, high-speed videos were captured through an optical microscope for direct observations of the spreading meniscus on both propagation directions. Shown in Fig. 4 are time-lapse images of the microscopic spreading meniscus on the easy wicking direction. The meniscus remains concave at each spreading stage captured on the video. Before the meniscus enters an opening between a tilted fin pair, its contacts to the side walls of the channel advance at high speeds while its instantaneous centerline velocity is close to zero or even slightly negative. This causes a rapid increase of the magnitude of the front curvature. Then, the highly curved meniscus generates a large pressure gradient which pulls the fluid through the opening rapidly. The spreading continues as the meniscus exits the narrow opening and appears to remain slightly concave. In comparison, shown in Fig. 5 are time-lapse images of the spreading meniscus on the hard wicking direction. The propagating front enters the first channels with a concave profile, but as soon as it reaches the exit of the narrow opening between the first pair of fins, the shape of the meniscus becomes convex and is pinned at the exit of the narrow opening between the fins. The pining of contact line at the edge of the fin-like structures can be explained by the Gibbs criterion [15,16], which states that a liquid meniscus at a sharp corner can exist at a contact angle anywhere between the advancing contact angles on the two surfaces intersecting to form the corner. Thus at the exit of the narrow opening between the fins, the meniscus must deform such that the advancing contact angle is reached on the downstream side of the fin before the meniscus can advance further.

In order to investigate the effects of wettability on asymmetric wicking of fluid through our micro-channels, the contact angle between the test fluid and the PDMS surface was tuned by varying the mixing ratio of IPA and water. The specific values of contact angles were experimentally measured and are presented in Fig. 6. As shown in this figure, the cosine of the contact angle, $\cos\theta$, was found to increase linearly with increasing IPA concentration in the mixture. Based on our simplified 2-D model, it is expected that the fluid will not spread in the hard wicking direction due to the

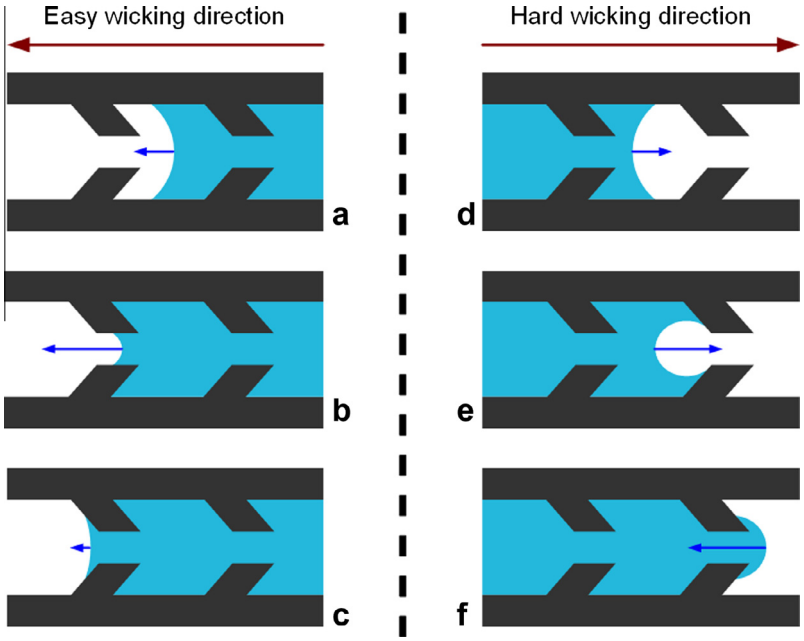

Fig. 3. Schematic diagrams of the asymmetric wicking mechanism based on a simplified 2D model. Top-view images representing consecutive stages of propagation of a wetting fluid (shown in blue) in a micro-channel (shown in black) on the easy direction (a–c) and the hard direction (d–f) of wicking are compared side-by-side. The arrows represent the strength and direction of the Laplace pressure at each stage. (For interpretation of the references to colour in this figure legend, the reader is referred to the web version of this article.)

positive-definite curvature of the meniscus, but the spreading of the fluid in the easy wicking direction can be controlled by the amount of IPA in the mixture. For a more detailed understanding of the wicking dynamics, plotted in Fig. 7 are the spread distances as functions of time for three IPA–water mixtures - 60% 80%, 90% IPA volume ratio, respectively – on the microfluidic device described in Table 1. Notice in the easy wicking direction, both the 80% IPA and the 90% IPA solutions wicked through but the wicking of the 60% IPA solution stopped midway in the micro-channels; in the hard wicking direction, only the 90% IPA solution wicked through, both the 60% IPA and the 80% IPA solution did not wick. It was found that, on this device, under open atmosphere, at least partial wicking was allowed on the easy direction for IPA percentage above 40%. Spreading was stopped on the hard direction unless IPA ratio was above 85%. Generally, the wicking speed on the easy direction decreases with decreasing IPA ratio of the mixture, because a lower IPA ratio corresponds to a higher contact angle and consequentially a smaller driving force that comes from a lower Laplace pressure. With a total channel length of approximately 6 mm, it took between 5 s and 20 s for a test fluid with IPA ratio higher than 70% to wick through.

Based on the data presented in Fig. 7, it is clearly that the speed of wicking in the easy direction decreased as the fluid front advanced. A log–log plot of the data presented in Fig. 8 shows a power-law dependence of the wicked distance with time. At long times, the characteristic power index for all the fluids converge to within the range of 0.55–0.60. This can be explained by a simple model of capillary action under the absence of gravity. Here a laminar channel flow is driven by a constant Laplace pressure, so the pressure drop across the length of the fluid column inside the capillary should be inversely proportional to the length of the column, L. Based on the Poiseuille equation [20], this pressure drop is proportional to the volumetric flow rate, or front velocity, V. Therefore,

$$V = \frac{dL}{dt} \propto \frac{1}{L}, \tag{2}$$

which gives $L \propto \sqrt{t}$. This means that the length of the wicking fluid column should grow as the square root of time, which is close to the scaling observed in the experiments. The small discrepancy in the characteristic power indexes between experimental extraction and theoretical prediction is likely due to the structural details of the channels or perhaps simply measurement errors. It is worth noting that, in Fig. 7, there is one wicking curve – 90% IPA in the hard wicking direction – which displays a more linear relationship between wicking distance and elapse time. This noticeable difference is believed to be due to the fact that the underlying mechanism which enables wicking (for wetting fluids with relatively low contact angles) on the hard direction is distinct from that on the easy direction. More detailed explanations will be provided in the following sections.

One question that needs to be addressed is why the 60% IPA solution only spread halfway down the micro-channels in the easy wicking direction before stopping. The simplified 2D model would suggest that if a fluid could initially wick into a structured microchannel, it should be able to wick all the way through the channel. Assuming the volume of fluid removed from the reservoir is small, which it is. This discrepancy between 2D theoretical prediction and experimental observation clearly indicates one or more important components are missing in the model. The two primary physical components that our 2D model ignores are the effect of evaporation, specifically the evaporation of the IPA, and the 3D effects at the leading edge of the spreading meniscus. The effects due to evaporation of the test fluid were examined by comparing open experiments to those performed in a solvent rich environment. For experiments in closed atmosphere, the whole glass slide on which the PDMS microfluidic device was placed was covered with a transparent polystyrene Petri-dish with drilled holes for needle access. A simple enclosure like this can also be implemented in biomedical or other applications of these devices where airborne contaminant can be an issue. As shown in Fig. 9, the environmental conditions can have a large impact on spreading. In experiments where the 60% IPA test fluid was allowed to spread in the easy wicking direction, under an open atmosphere, the test fluid was

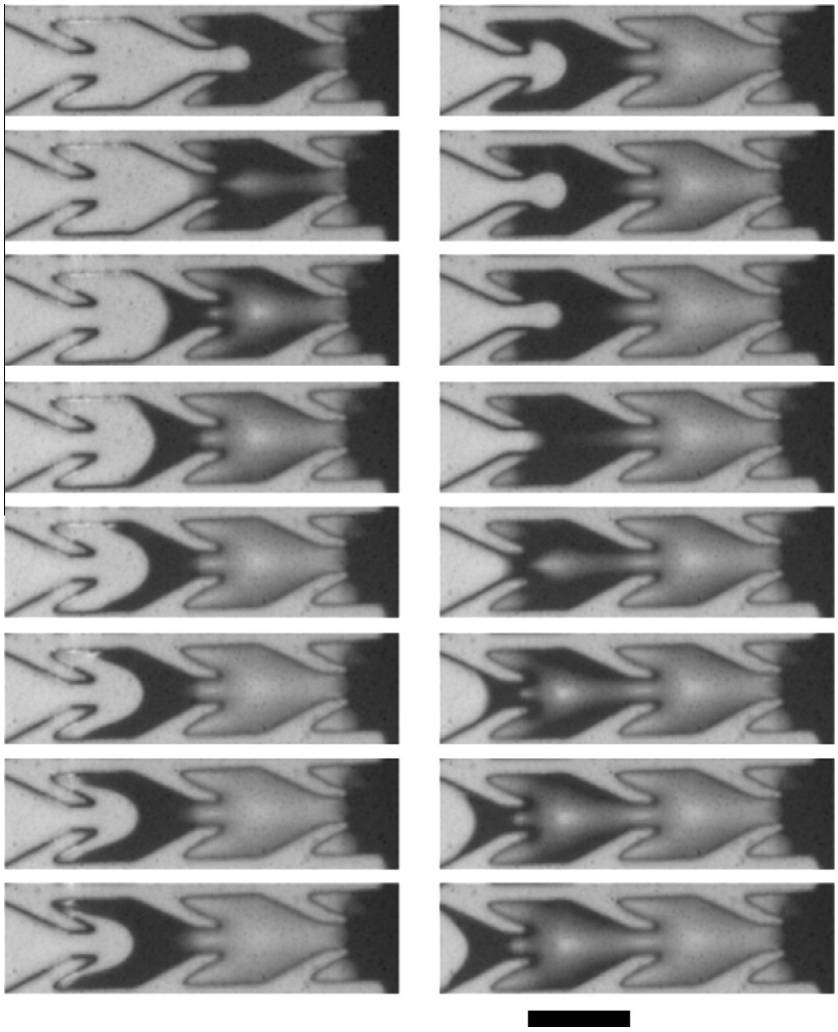

Fig. 4. Sequential frames from a high-speed video of fluid propagation on the easy wicking direction (from right to left on each image). The chronological order of the images is first the left column then the right column. Individual frames were taken 1 ms apart. The scale-bar at the bottom represents 100 μm.

observed to wick only half-way through the channels. If, however, the PDMS device was covered with a Petri-dish inside which the environment was saturated with equilibrium vapor of the same IPA and water mixture, the same 60% IPA test fluid was found to wick completely through the micro-channel array. In experiments where the test fluid IPA ratio was 70%, covering the PDMS device increased the wicking speed. These experiments confirmed that the higher evaporation rate of IPA compared to water leads to lowering of IPA concentration locally at the fluid front. The increase contact angle results in a transition from a concave to a convex meniscus causing the propagation of the fluid front to stall. It was found by experiment that, under a solvent vapor saturated environment, a test fluid of 40% IPA ($\theta \approx 61^\circ$) could wick into the micro-channels while a test fluid of 35% IPA ($\theta \approx 68^\circ$) could not wick into the channels at all.

As shown in Fig. 7, the 90% IPA test fluid was observed to completely wick through the micro-channels in both the easy and the hard wicking directions. The entire wicking process took about 60 s in the hard wicking direction compared to about 5 s in the easy direction. Other than evaporation effects, this is another example of how the simplified 2D model, while in many cases is adequate for explaining qualitative trends, cannot capture some of the important aspects of physics. This observation is not a result of evaporation, but rather a case where 3D effects need to be taken into account. To obtain a more accurate quantitative prediction of the wicking behavior, 3D simulations based on the Surface Evolver were employed [21–23]. Two representative 3D menisci obtained from the simulations, one spreading in the easy wicking direction and the other spreading in the hard wicking direction, are shown in Fig. 10. In general, the shapes of the 3D menisci computed by simulations are not fundamentally distinct from what were expected using the 2D model. The major difference is the a sloped front profile on the vertical plane as a result of the micro-channel having a wet, solid bottom and a top open to air. In most cases, these differences are not enough to keep the simplified 2D model from providing satisfactory qualitative predictions consistent with the experimental observations of asymmetric wicking behaviors. There are, however, a number of limiting cases where predicting the 3D characteristics of the meniscus is critical to understanding the observed wetting behavior. One such case is a special example of groove instability under geometric confinements which occurs where the vertical walls meet the floor of the micro-channels, as illustrated in Fig. 11. This instability has been examined in a number of previous studies and is known to occur at a critical combination of geometry and contact angle [24–26]. For a 90° wedge, with side-walls exactly perpendicular to the floor, the critical contact angle is 45°. Below this angle, the fluid will wick indefinitely along the wedge. The critical contact angle decreases as the inner angle of the wedge increases. One of the ramifications of this instability is that it enables wicking on the

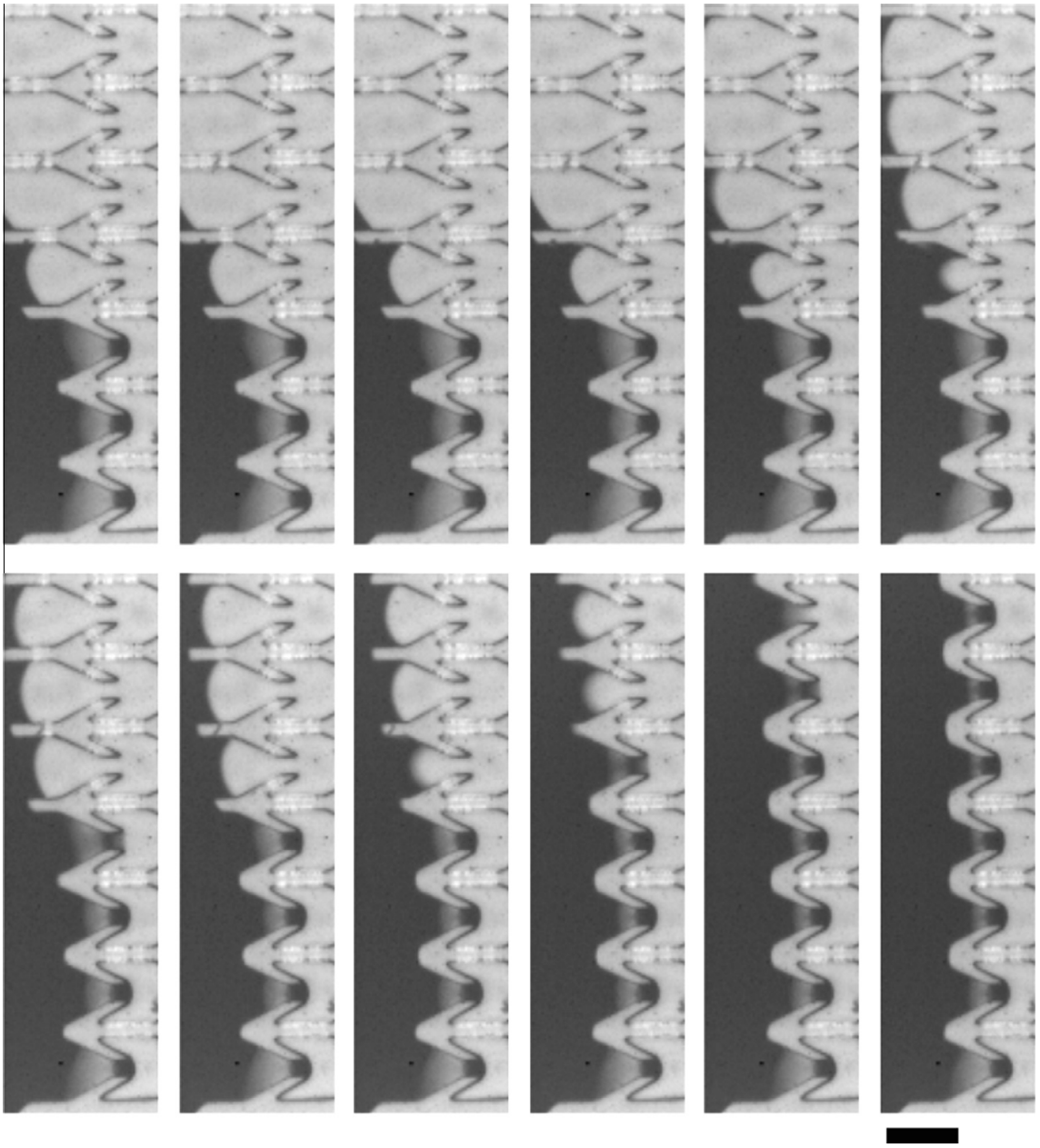

Fig. 5. Sequential frames from a high-speed video of fluid (dark color) propagation on the hard wicking direction (from left to right on each image). The chronological order of the images is first the top row then the bottom row. Individual frames were taken 1 ms apart. The scale-bar at the bottom represents 100 μm.

hard direction for fluids with relatively low contact angles even though our simplified 2D model would exclude it. As shown in Fig. 10, this is because the groove instability allows the meniscus to extend along the lower front corners of the micro-structures. When the meniscus reaches the inside wall of the channel, the boundary condition is altered to one which favors forward wicking and the front moves down the channel to the next feature, albeit relatively slowly. This instability-enabled wicking mechanism is responsible for the distinct dynamics observed on 90% IPA in the hard wicking direction. Specifically, the phase where the meniscus stretch along the corner is a lot slower than that of propagation through the straight portion of channel between the fins. Therefore, the time limiting phase is meniscus stretching, which is relatively insensitive to the total length of the fluid column because fluid supply at the openings between fins is fast. This results at approximately constant wicking velocity and a linear distance-time relationship as mentioned previously. Quantitatively, the average hydraulic diameter, $d_h = 4 \cdot area/perimeter$, can be estimated for each of the two spreading phases and then compared. For the meniscus stretching phase, the average cross-section of the fluid can be roughly approximated as a right-angle triangle with the length of both catheti equal to $h/2$, or half the height of the structures. This results in a hydraulic diameter for the stretching phase $d_{h,str} \approx 16.4$ μm. For the propagation through the straight section phase, the cross-section of the fluid can be roughly approximated as a rectangle with the length of two sides equal to the height of the structures, h, and the opening width, a, respectively. This results in a hydraulic diameter for propagating phase $d_{h,pro} \approx 29.5$ μm. The volumetric flow rate of a Poiseuille flow is proportional to the fourth power of the hydraulic diameter, $\frac{Q_{pro}}{Q_{str}} = \left(\frac{d_{h,pro}}{d_{h,str}}\right)^4 \approx 10.5$. This result indicates that, for the same 90% IPA fluid, it takes about ten times longer to fill the channels in the hard wicking direction than in the easy wicking direction,

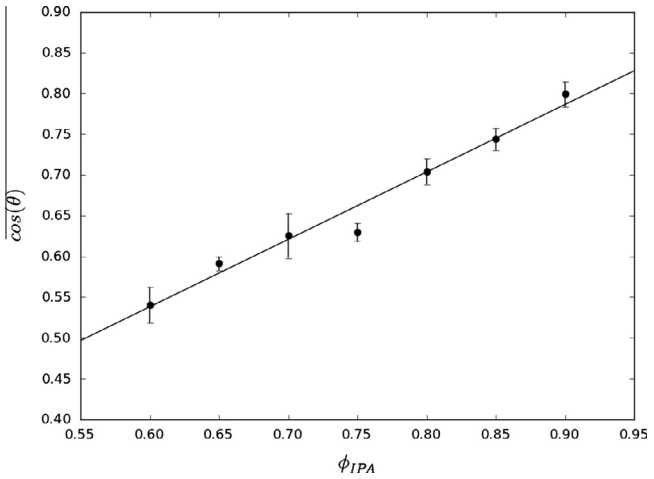

Fig. 6. Contact angle between test fluid and PDMS surface varies as a function of IPA volume ratio.

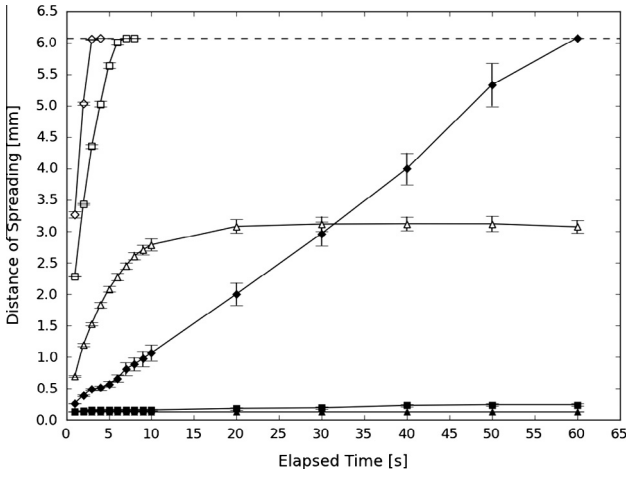

Fig. 7. Distance of spreading as a function of time for a series of different IPA–water mixtures. The data include: 60% IPA (triangle, △), 80% IPA (square, □), 90% IPA (diamond, ♢) test fluids on the device described in Table 1. All experiments were performed open to atmosphere. The open symbols represent wicking in the easy direction and the closed symbols represent wicking in the hard direction. The dashed-line indicates the total length of the channels.

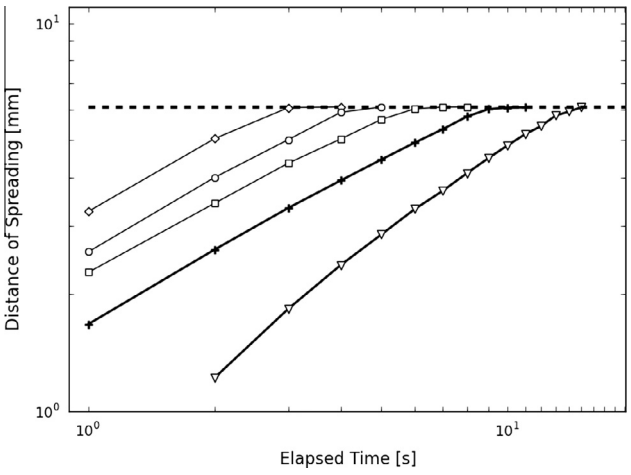

Fig. 8. Wicking on the easy direction shown at a log–log scale. The dashed-line indicates the total length of the channels. Slopes of the fit-lines varied between 0.55 and 0.60 for the 80% IPA (□), 85% IPA (○), and 90% IPA (♢) test fluids under open atmosphere, and at long times for the 70% IPA (+) and 60% IPA (▽) test fluids under vapor saturated environment.

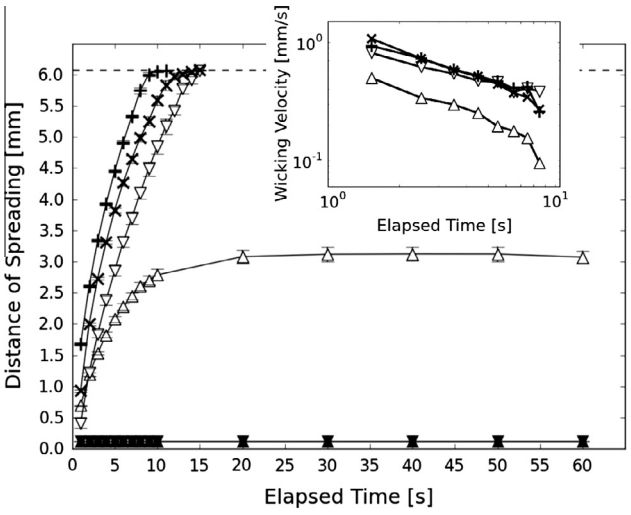

Fig. 9. Distance of spreading of the wicking front as a function of time. The dashed-line indicates the total length of the channels. This plot quantifies the wicking process of 60% IPA fluids under open (△) and closed (▽) atmosphere, and 70% IPA fluids under open (×) and closed (+) atmosphere for the microfluidic device described in Table 1. The wicking velocities (in log–log scale) are presented in the inset. The velocity data is all found to scale roughly as $V \propto t^{-0.5}$.

which is in fairly good agreement with the experimental measurements.

So far, all the discussions have been based on the same device structure whose geometric parameters are listed in Table 1. In these experiments, the only parameter that has been varied was the contact angle and interfacial tension. The next step was to investigate the effects of variation of each geometric parameter of the device structure on the wicking behavior. A range of geometric parameters tested are presented in Table 1. Qualitatively, it was observed that lowering the height, h, of the structures to $h = 22$ μm, while keeping other parameters the same, led to a lower degree of wicking asymmetry by both promoting wicking on the hard direction and diminishing wicking on the easy direction. This agrees with the intuition that 3D effects are more pronounced on structures with lower aspect ratios, because the Laplace pressure is dictated by the mean curvature, which is dictated by the two principle curvatures. Moreover, a smaller value of opening width, a, led to a higher degree of wicking asymmetry, as one would predict based on the simplified 2D model. In terms of the tilting angle, ϕ, on one hand it is better to have smaller tilting angle to induce a large front curvature difference between opposite spreading directions, but on the other hand, the 3D effects makes it necessary to also consider the spacing between consecutive fins along the microchannels and between the fins and the side-wall of the channels. This restricts tilting angle within a certain range based on the values of the other geometric parameters d, a, and w. We observed that a 27° tilting angle produced larger wicking asymmetry, in terms of the extend and speed, than a 45° tilting angle in most cases.

The capability of precisely calculating the 3D meniscus shape (by using simulations based on the Surface Evolver) allows for a model that can more accurately predict the wicking behavior and to establish design rules for developing and optimizing unidirectional wicking channels. Here we examined the easy and hard wicking directions separately. In the hard wicking direction, our simulations agree quite well with the predictions of $\theta_{crit} = 45°$

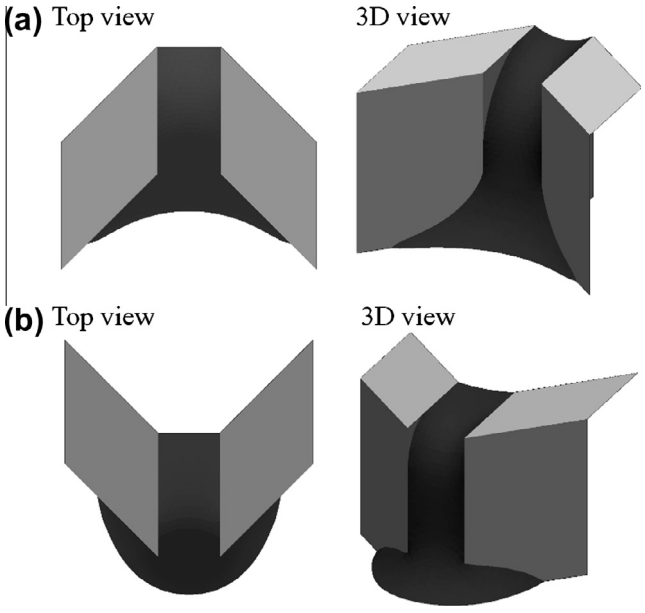

Fig. 10. Representative 3D menisci (shown in dark color) resulted from Surface Evolver simulations of a wetting fluid ($\theta = 48°$) at the opening between tilted arms on opposite sides. A top view and a 3D view of the menisci formed when the fluid spreads on (a) the easy wicking and (b) the hard wicking directions are included.

below which the fluid will wet as a result of the groove instability. This critical contact angle is only affected by the angle at which the fin-like structures meet the bottom of the channel. In the easy direction, our simulations predict that like in the hard direction, for $\theta < 45°$, fluid always wick. For $\theta > 45°$, the fluid can wick with proper design of the channel geometry. For a fixed channel height, our simulations confirm that the wicking behavior is mainly controlled by the tilting angle of the fins, ϕ. Results of our simulations suggest that the projected (from the top view) contact angle, θ_{proj} (schematically defined in Fig. 12a), can be used as an excellent predictor of whether the fluid will wick into the micro-channels. In the 2D model represented by Fig. 3, the dynamics of the wetting fluid on the easy wicking direction is controlled by the sum of ϕ and θ. Taking into account the 3D effect, θ should be replaced by θ_{proj}. The combination of ϕ and θ_{proj} can be represented by the front forward angle, ω, as shown in Fig. 13, and the criterion for wicking, from the 2D viewpoint, becomes whether $\omega = \phi + \theta - \pi/2 < 0°$. Clearly, this criterion is only true when the meniscus has zero curvature on the vertical direction. The projected contact angle can be calculated from Surface Evolver simulations or it can be approximated a priori from the advancing contact angle and some geometric arguments. When one zooms in close enough to the corner where the propagating front meets the tilted fin, one observes that the tip of the fluid forms a tetrahedron (because the local curvature of any point on the meniscus has to be finite), as shown in Fig. 12b. The shape of this tetrahedron only depends on θ, and once the shape is determined, θ_{proj} can be calculated as:

$$\cos\theta_{proj} = \frac{1}{\tan\theta}. \tag{3}$$

Good agreements can be demonstrated between the simulation results and the analytical solution. A strong correlation between the front forward angle, ω, and the fluid behavior (whether or not advance) can be concluded. This indicates that, under a fixed channel height, the curvature on the vertical direction is approximately unchanged. The effect due to this vertical curvature is shifting the criterion for fluid wicking from $\omega = 0°$ to approximately $\omega = 6°$. From

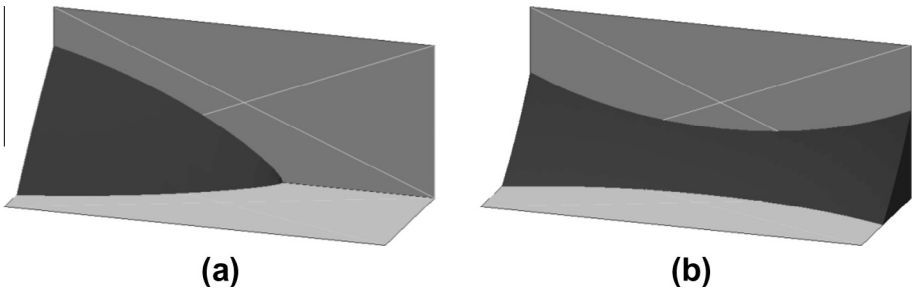

Fig. 11. Illustration of the groove instability which occurs at a 90° wedge. 3D menisci (shown in dark color) of wetting fluids with contact angles of (a) 50° and (b) 40° are included. When the contact angle is above the critical contact angle, as shown in (a), the fluid spreads a finite distance along the wedge. When the contact angle is below the critical contact angle, as shown in (b), the fluid spreads along the wedge indefinitely.

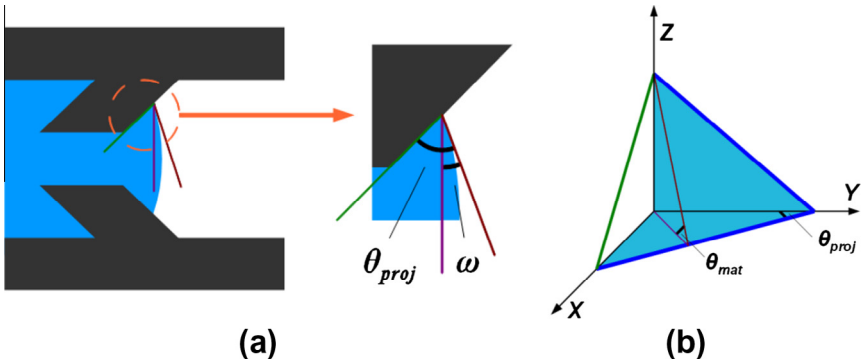

Fig. 12. Calculation of projected contact angle, θ_{proj}. (a) Schematics of the projected contact angle, θ_{proj}, and the front forward angle, ω, from the top view. (b) Schematics of the tetrahedron formed at the tip of the advancing front.

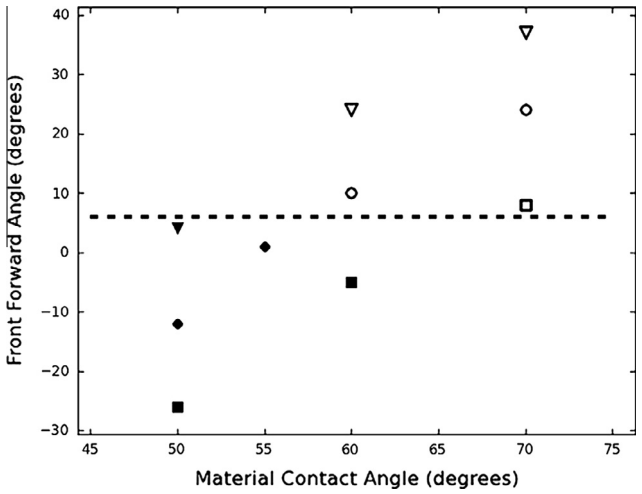

Fig. 13. Plot of the front forward angle, ω, as a function of the material contact angle θ_{mat} for fin-tilting angle of 60° (▼), 45° (●), and 30° (■). Solid symbols denote spontaneous advancing while hollow symbols represent cases where the fluid front does not propagate. The dashed line corresponds to $\omega = 6°$, which is the estimated division between the propagating and non-propagating meniscus cases..

this set of simulation results, it is clear that the 2D model captured most of the qualitative trends and can be used to conservatively predict wicking to within a few degrees in contact or fin angle. The full 3D simulation provides improvements for the quantitative predictions, but at a cost of complexity and time.

4. Conclusions

The ability to passively control the spreading of fluids is of tremendous importance in the development of microfluidic devices and in the understanding of flow within them. In this paper, we introduced a new type of open microfluidic channels that are capable of producing asymmetric wicking for a wide range of wetting fluids. This "microfluidic diode" behavior is based on direction-dependent Laplace pressure induced by asymmetric structures. Specifically, an array of ten parallel micro-channels were fabricated with the addition of periodic tilted fins that extended into the channels at a specific angle and period. A mixture of IPA and water introduced from a reservoir was shown to rapidly wick through the channels only in a predefined direction. Spreading of the same fluid in the opposite direction was completely prohibited by the presence of the tilted fins. Detailed examinations of the basic mechanism which produces this effect were predicted by a simple 2D theory and investigated in depth by full 3D simulations. We found that for test fluids of many different IPA–water mixing ratios, the simplified 2D model was adequate to provide qualitative predictions. For test fluids with low IPA ratios, evaporation effects that led to changing of composition needed to be included in the mechanism. For test fluids with high IPA ratios, groove instability of the 3D fluid system can quantitatively modify the wicking behavior. Multiple physical, chemical, and geometric parameters were varied to systematically study their individual effects on the wicking behaviors. It was found that a lower fin-tilting angle, a larger fin length or a smaller opening width, and a larger structure height all resulted in a higher degree of wicking asymmetry.

Acknowledgments

The authors gratefully acknowledge the funding from the National Science Foundation's Center for Hierarchical Manufacturing (Grant No. CMMI-1025020) at the University of Massachusetts Amherst. The authors would also like to acknowledge Professor Mark T. Tuominen for the helpful discussions.

References

[1] G.M. Whitesides, The origins and the future of microfluidics, Nature 442 (2006) 368–373.
[2] M.A. Burns et al., An integrated nanoliter DNA analysis device, Science 282 (1998) 484–487.
[3] D.J. Beebe, G.A. Mensing, G.M. Walker, Physics and applications of microfluidics in biology, Annu. Rev. Biomed. Eng. 4 (2002) 261–286.
[4] D. Erickson, D.Q. Li, Integrated microfluidic devices, Anal. Chim. Acta 507 (2004) 11–26.
[5] T.M. Squires, S.R. Quake, Microfluidics: fluid physics at the nanoliter scale, Rev. Mod. Phys. 77 (2005) 977–1026.
[6] M.A. Unger, H.P. Chou, T. Thorsen, A. Scherer, S.R. Quake, Monolithic microfabricated valves and pumps by multilayer soft lithography, Science 288 (2000) 113–116.
[7] D.J. Laser, J.G. Santiago, A review of micropumps, J. Micromech. Microeng. 14 (2004) R35–R64.
[8] A.W. Martinez, S.T. Phillips, G.M. Whitesides, Three-dimensional microfluidic devices fabricated in layered paper and tape, Proc. Natl. Acad. Sci. USA 105 (2008) 19606–19611.
[9] J.L. Osborn et al., Microfluidics without pumps: reinventing the T-sensor and H-filter in paper networks, Lab Chip 10 (2010) 2659–2665.
[10] D.R. Ballerini, X. Li, W. Shen, An inexpensive thread-based system for simple and rapid blood grouping, Anal. Bioanal. Chem. 399 (2011) 1869–1875.
[11] A.W. Martinez et al., Programmable diagnostic devices made from paper and tape, Lab Chip 10 (2010) 2499–2504.
[12] H. Chen, J. Cogswell, C. Anagnostopoulos, M. Faghri, A fluidic diode, valves, and a sequential-loading circuit fabricated on layered paper, Lab Chip 12 (2012) 2909–2913.
[13] T.I. Kim, K.Y. Suh, Unidirectional wetting and spreading on stooped polymer nanohairs, Soft Matter 5 (2009) 4131–4135.
[14] K.H. Chu, R. Xiao, E.N. Wang, Uni-directional liquid spreading on asymmetric nanostructured surfaces, Nat. Mater. 9 (2010) 413–417.
[15] M.L. Blow, H. Kusumaatmaja, J.M. Yeomans, Imbibition through an array of triangular posts, J. Phys. Condens. Matter 21 (2009) 464125.
[16] M.L. Blow, J.M. Yeomans, Anisotropic imbibition on surfaces patterned with polygonal posts, Philos. Trans. Roy. Soc. A 369 (2011) 2519–2527.
[17] H. Kusumaatmaja, C.M. Pooley, S. Girardo, D. Pisignano, J.M. Yeomans, Capillary filling in patterned channels, Phys. Rev. E 77 (2008) 067301.
[18] D.C. Duffy, J.C. McDonald, O.J.A. Schueller, G.M. Whitesides, Rapid prototyping of microfluidic systems in poly(dimethylsiloxane), Anal. Chem. 70 (1998) 4974–4984.
[19] J.C. McDonald, G.M. Whitesides, Poly(dimethylsiloxane) as a material for fabricating microfluidic devices, Accounts Chem. Res. 35 (2002) 491–499.
[20] F.M. White, Fluid Mechanics, seventh ed., Mcgraw-Hill Series in Mechanical Engineering, 2011. ISBN:9780077422417.
[21] K.A. Brakke, The surface evolver, Exp. Math. 1 (1992) 141–165.
[22] K.A. Brakke, The surface evolver and the stability of liquid surfaces, Philos. Trans. Roy. Soc. Lond. Ser. A 354 (1996) 2143–2157.
[23] Y. Chen, B. He, J.H. Lee, N.A. Patankar, Anisotropy in the wetting of rough surfaces, J. Colloid Interf. Sci. 281 (2005) 458–464.
[24] K. Rejmer, S. Dietrich, M. Napiorkowski, Filling transition for a wedge, Phys. Rev. E 60 (1999) 4027–4042.
[25] M. Kitron-Belinkov, A. Marmur, T. Trabold, G.V. Dadheech, Groovy drops: effect of groove curvature on spontaneous capillary flow, Langmuir 23 (2007) 8406–8410.
[26] J. Feng, J.P. Rothstein, Simulations of novel nanostructures formed by capillary effects in lithography, J. Colloid Interf. Sci. 354 (2011) 386–395.